Single Image De-Hazing Using Globally Guided Image Filtering

Zhengguo Li, *Senior Member, IEEE*, and Jinghong Zheng, *Member, IEEE*

Abstract—Local edge-preserving smoothing techniques such as guided image filtering (GIF) and weighted guided image filtering (WGIF) could not preserve fine structure. In this paper, a new globally guided image filtering (G-GIF) is introduced to overcome the problem. The G-GIF is composed of a global structure transfer filter and a global edge-preserving smoothing filter. The proposed filter is applied to study single image haze removal. Experimental results show that fine structure of the dehazed image is indeed preserved better by the proposed G-GIF and the dehazed images by the proposed G-GIF are sharper than those dehazed images by the existing GIF.

Index Terms—Globally guided image filtering, structure transfer, edge-preserving smoothing, single image haze removal.

I. Introduction

THE execution of visual activities such as object detection and recognition depends heavily on the perception of outdoor natural scenes. Unfortunately, images of outdoor scenes are often degraded in bad weather conditions such as haze, fog, smoke, rain and so on. The light is blended with ambient light reflected from other directions into the line of sight by atmospheric particles. The irradiance received by the camera from the scene point is attenuated along the line of sight. As such, the objects captured under the bad weather conditions suffer from low contrast, faint color, and shifted luminance [1]. Haze removal can significantly increase the contrasts of the objects, and correct the color distortion caused by the airlight. Therefore, haze removal is highly demanded in image processing and computer vision applications [2].

Many single image haze removal algorithms were proposed due to their broad applications. Based on an observation that a haze-free image has higher contrast than its haze image, an interesting single image haze removal algorithm was proposed in [3] by maximizing the local contrast of the restored image using markov random field. Although the algorithm in [3] is able to achieve visually compelling results, it tends to produce over-saturated images which might not be physically valid. A haze image is interpreted by Fattal in [4] through an image formation model that accounts for both surface shading and scene transmission. Under an assumption that the transmission

and surface shading are locally uncorrelated, the airlight-albedo ambiguity is resolved. The algorithm in [4] produced impressive results except in presence of heavy haze. Inspired by the widely used dark-object subtraction technique [5], a novel dark channel prior based haze removal algorithm was proposed in [6] and [7]. The dark channel prior is based on an observation that it is very often that some pixels of haze-free outdoor images have very low intensity in at least one color (RGB) channel. The algorithm is physically valid and can handle distant objects even in images with heavy haze. However, noise in bright regions including the sky could be amplified by using the algorithm in [6] and [7] even though a lower bound was introduced for the transmission map in [6] and [7]. Based on observations that the color of the scene fades under the influence of the haze and the brightness increases at the same time producing the high value of the difference, a simple color attenuation prior was proposed in [8], and a linear model was then built up to represent the relationship between the depth and the brightness as well as the saturation using the prior. The linear model was finally adopted to design a single image haze removal algorithm with the help of the guided image filtering (GIF) in [7]. The algorithm in [8] is simple and it also avoids amplification of noise in the sky region. In addition, the haze is removed well if it is light. However, the quality of the dehazed images needs to be improved if the haze is heavy. This is because the coefficients of the linear model and the scattering coefficient of the atmosphere are fixed for the algorithm in [8] while their values should be adaptive to the haze degree of the input image. It is interesting but challenging to properly determine the coefficients of the linear model and the scattering coefficient of the atmosphere for the algorithm in [8]. Inspired by an observation in [9] that single image haze removal can be regarded as a type of spatially varying detail enhancement, a neat framework was proposed in [11] by introducing a local edge-preserving smoothing based method to estimate the transmission map of a haze image. However, local edge-preserving smoothing techniques such as the GIF in [7] and the weighted GIF (WGIF) in [9] could over smooth images [12], especially in areas of fine structure. An example is given in Fig. 1. The GIF in [7] and the WGIF in [9] are adopted to study single image haze removal. As shown in the zoom-in regions, the hair of the human subject is over smoothed by both the GIF and the WGIF. Therefore, both the GIF and the WGIF could not preserve the fine structure even though they are very simple.

In this paper, a fast globally guided image filter (G-GIF) is introduced to address the problem. The proposed G-GIF is

Fig. 1. Comparison of the GIF, the WGIF and the G-GIF. (a) a haze image; (b) a dehazed image by the GIF; (c) a dehazed image by the WGIF; (d) a dehazed by the G-GIF. Both the GIF and the WGIF over smooth the hair of the human subject as illustrated in the zoom-in regions while the problem is overcome by the proposed G-GIF.

inspired by the GIF in [7], the WGIF in [9], and the gradient domain image processing algorithms in [10], [13], and [14]. Two major objectives of the GIF and WGIF are: 1) to transfer the structure of the guidance image to the input image; and 2) to smooth the transferred image so as to produce the output image. Both the objectives are achieved simultaneously in the GIF and WGIF. They are achieved separately in the proposed G-GIF. The proposed filter is composed of a global structure transfer filter and a global edge-preserving smoothing filter. Inputs of the structure transfer filter are an image to be filtered and a guidance vector field. The structure is defined by the guidance vector field and it is transferred to the image to be filtered by the structure transfer filter. Unlike the GIF in [7] and the WGIF in [9], the structure transfer filter is formulated as a quadratic optimization problem. Unlike the gradient domain image processing algorithms in [13] and [14], the structure filter is formulated in the hybrid gradient and image domain. As such, the proposed hybrid optimization problem can be easily solved by using the separating approach in [15] even though it is a global optimization problem while the separating approach is not applicable to the gradient domain image processing algorithms in [13] and [14]. The speed of the structure transfer filter is thus comparable to those of the GIF in [7] and the WGIF in [9], and is much faster than the gradient domain image processing algorithms in [13] and [14]. The proposed edge-preserving smoothing filter is inspired by the weighted least square (WLS) filter in [16] and the detail extraction problem in [17]. Inputs of the smoothing filter are an image to be smoothed and the guidance vector field. Similar to the structure transfer filter, the smoothing filter is also formulated as a quadratic optimization problem. It is worth noting that the WLS filter in [16] is a special case of the proposed edge-preserving smoothing filter. Due to the separating approach, the speed of the smoothing filter is also comparable to those of the GIF in [7] and the WGIF in [9]. As illustrated in Fig. 1, the proposed G-GIF preserves the fine structure better than the GIF and WGIF.

The G-GIF is then applied to study single image haze removal. The proposed haze removal algorithm is based on the concepts of minimal color channel [19]–[21] and simplified dark channel in [9]. The simplified dark channel is decomposed into a base layer and a detail layer via the proposed G-GIF, and the base layer is used to estimate the transmission map. To avoid introducing artifacts to the dehazed image, the structure of the base layer (or the structure of the transmission map) is required to match the structure of the haze image. Since the structure of the haze image is preserved better by the minimal channel than the simplified dark channel [11], the minimal color channel is selected to generate the guidance vector field. Once the transmission map is estimated from the base layer, it can be used to recover the haze image. Experimental results show that the dehazed images by the proposed algorithm are sharper than those dehazed images by the algorithms in [7], [8], and [11]. It should be pointed out that the computational cost of the proposed algorithm is about the double of the algorithms in [7], [8], and [11]. Overall, there are two major contributions in this paper. One is the proposed G-GIF which preserves fine structures better than the GIF and WGIF. The other is a new single image haze removal algorithm based on the proposed G-GIF which can be applied to improve the sharpness of dehazed images.

The rest of this paper is organized as follows. Limitation of the GIF and WGIF is given in Section II. The detail of the proposed G-GIF is provided in Section III. Section IV includes an application of the proposed G-GIF in single image haze removal. Experimental results are given in Section V to illustrate the efficiency of the proposed haze removal algorithm. Concluding remarks are provided in Section VI.

II. LIMITATION OF THE GIF AND WGIF

In both the GIF [7] and the WGIF [9], a guidance image G is used which could be identical to the image X to be filtered. It is assumed that the output image $\hat{Z}$ is a linear transform of G in a predefined window $\Omega_\zeta(p')$:

$$\hat{Z}(p) = a_{p'}G(p) + b_{p'}, \quad \forall p \in \Omega_\zeta(p'), \quad (1)$$

where $\Omega_\zeta(p')$ is a square window centered at the pixel p' of a radius ζ. $a_{p'}$ and $b_{p'}$ are two constants in the window $\Omega_\zeta(p')$.

The values of $a_{p'}$ and $b_{p'}$ in the GIF [7] are then obtained by minimizing a cost function $E(a_{p'}, b_{p'})$ which is defined as

$$E = \sum_{p \in \Omega_\zeta(p')} [(a_{p'}G(p) + b_{p'} - X(p))^2 + \lambda a_{p'}^2], \quad (2)$$

where λ is a regularization parameter penalizing large $a_{p'}$.

An edge-aware weighting $\Gamma_G(p')$ is defined in the WGIF [9] by using local variances of 3×3 windows of all pixels as

Fig. 2.   Limitation of the WGIF. (a) $\zeta = 7$; (b) $\zeta = 15$; (c) $\zeta = 30$; and (d) $\zeta = 60$. The morphological artifacts are reduced but the hair of the human subject becomes over smoothed if the value of ζ is increased.
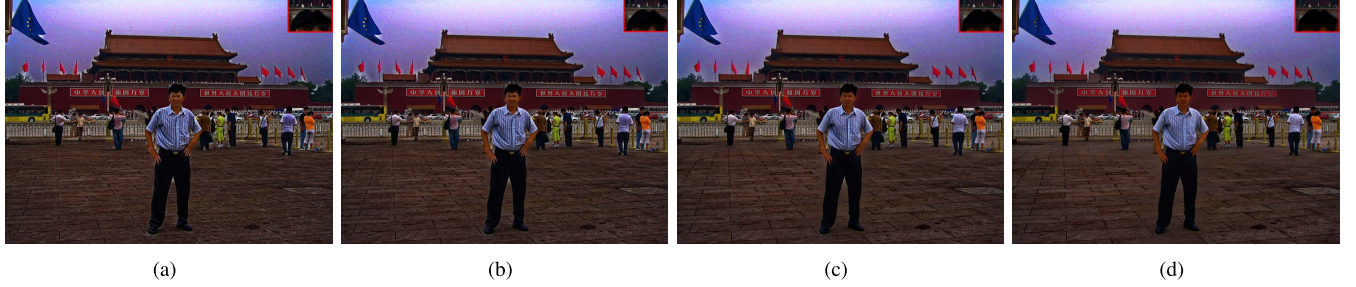

Fig. 3.   Limitation of the GIF. (a) $\zeta = 7$; (b) $\zeta = 15$; (c) $\zeta = 30$; and (d) $\zeta = 60$. The morphological artifacts are reduced but the hair of the human subject becomes over smoothed if the value of ζ is increased.

follows:

$$\Gamma_G(p') = \frac{1}{N} \sum_{p=1}^{N} \frac{\sigma_{G,1}^2(p') + \varepsilon}{\sigma_{G,1}^2(p) + \varepsilon}, \qquad (3)$$

where ε is a small constant and its value is selected as $(0.001 \times L)^2$ while L is the dynamic range of the input image.

The edge-aware weighting $\Gamma_G(p')$ in Equation (3) is incorporated into the cost function $E(a_{p'}, b_{p'})$ in Equation (2). As such, the values of $a_{p'}$ and $b_{p'}$ in the WGIF [9] are then obtained by minimizing a new cost function $E(a_{p'}, b_{p'})$ which is defined as

$$E = \sum_{p \in \Omega_\zeta(p')} [(a_{p'}G(p) + b_{p'} - X(p))^2 + \frac{\lambda}{\Gamma_G(p')} a_{p'}^2]. \qquad (4)$$

The optimal values of $a_{p'}$ and $b_{p'}$ are computed by solving the optimization problem (2) or the optimization problem (4). The output image $\hat{Z}(p)$ is finally given as follows: [9]

$$\hat{Z}(p) = \bar{a}_p G(p) + \bar{b}_p, \qquad (5)$$

where $\bar{a}_p$ and $\bar{b}_p$ are the mean values of $a_{p'}$ and $b_{p'}$ in the window computed as

$$\bar{a}_p = \frac{1}{|\Omega_\zeta(p)|} \sum_{p' \in \Omega_\zeta(p)} a_{p'} \qquad (6)$$

$$\bar{b}_p = \frac{1}{|\Omega_\zeta(p)|} \sum_{p' \in \Omega_\zeta(p)} b_{p'}, \qquad (7)$$

and $|\Omega_\zeta(p')|$ is the cardinality of $\Omega_\zeta(p')$.

As an illustration, both the GIF and the WGIF are applied to study single image haze removal. Four different choices of ζ are tested and they are 7, 15, 30, and 60. Readers are
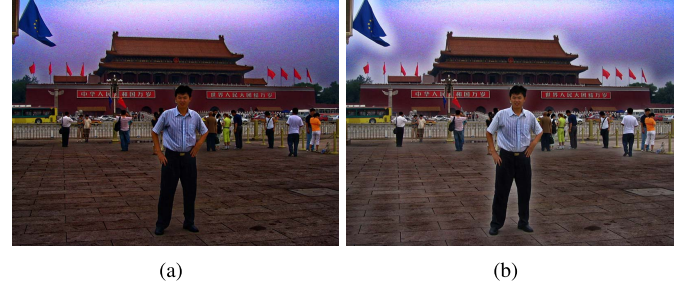

Fig. 4.   Effect of the maximal filter. (a) a dehazed image with the maximal filter; and (b) a dehazed image without the maximal filter. The morphological artifacts are reduced by the maximal filter but the hair of the human subject is further smoothed heavily.

invited to view the electronic version of the full-size figures in order to better appreciate the differences among images. It is shown in Fig. 2 that the morphological artifacts are reduced if the value of ζ is increased. However, the hair of the human subject becomes smoothed or even over smoothed when the value of ζ is increased. The same phenomenon is observed for the GIF in Fig. 3. It is worth noting that the maximal filter is enabled for all the experimental results in Fig. 3. Here the maximal filter is obtained by replacing the minimal operation in the equation (21) by the maximal operation. It is shown in Fig. 4 that the morphological artifacts are indeed reduced by the maximal filter. Unfortunately, the hair of the human subject is further over-smoothed by it. The maximal filter is thus not enabled provided that it is specified in this paper. The WGIF is taken as example to show the effect of the average operations in the Equations (6) and (7). It is shown in Fig. 5 that the fine structures are preserved better while the morphological artifacts become more visible by

Fig. 5. Dehazed images by the WGIF without the average operations (6) and (7). (a) $\zeta = 7$; (b) $\zeta = 15$; (c) $\zeta = 30$; and (d) $\zeta = 60$. The fine structures are preserved better by disabling the average operations (6) and (7) while the morphological artifacts become more visible.

disabling the average operations in the Equations (6) and (7). Clearly, both the GIF [7] and the WGIF [9] can over smooth images, especially in areas of fine structures. This is due to the large value of ζ and the average operations in the Equation (6) and (7). In the next subsection, a new G-GIF is proposed to address the problem.

III. GLOBALLY GUIDED IMAGE FILTERING

Inspired by the GIF in [7], the WGIF in [9], the gradient domain image processing algorithms in [10], [13], and [14], the WLS filter in [16] and the quadratic optimization problem in [17], a new type of GIFs is proposed in this section. Unlike the GIF in [7] and the WGIF in [9], the proposed filter is a global filter and it is thus called the G-GIF. Inputs of the proposed G-GIF are an image to be filtered and a guidance vector field while inputs of the GIF and WGIF are an image to be filtered and a guidance image. The structure is defined by the guidance vector field. The proposed G-GIF is composed of a global structure transfer filter and a global edge-preserving smoothing filter. The function of the structure transfer filter is to transfer the predefined structure to the image to be filtered while the function of the smoothing filter is to smooth the transferred image so as to produce the output image.

The structure transfer filter is inspired by the GIF in [7], the WGIF in [9], and the gradient domain image processing algorithms in [10], [13], and [14]. The inputs of the structure transfer filter are an image to be filtered and a guidance vector field. The structure to be transferred is defined by the the guidance vector field. The objective of the structure transfer filter is to transfer the structure to the image to be filtered. The structure transfer filter is formulated as a global optimization problem. The cost function is composed of two terms. One term is in image domain and it measures the fidelity of the output image to the image to be filtered. The other is in gradient domain and it specifies the structure of the output image. The former is defined as

$$E_1(O, X) = \sum_p (O(p) - X(p))^2, \qquad (8)$$

where X is an image to be filtered. The term $E_1(O, X)$ implies that the output image O is required to approximate the image to be filtered as much as possible.

Let $V = (V^h, V^v)$ be the guidance vector field. The latter is defined as

$$E_2(O, V) = \sum_p \|\nabla O(p) - V(p)\|^2, \qquad (9)$$

where ∇O is the gradient field of the output image O. The term $E_2(O, V)$ means that the structure of the output image O matches the guidance vector filed as much as possible [14].

The overall cost function is computed as

$$E(O) = \lambda E_1(O, X) + E_2(O, V), \qquad (10)$$

where λ is a non-negative constant and its function is to obtain a trade-off between the two terms.

It should be pointed out that 1) the proposed cost function $E(O)$ is the same as the cost function in [14] if the value of λ is 0; and 2) the proposed cost function $E(O)$ is similar to the cost function in [17] when all pixel values in the input image are zeros. This implies that the cost functions in [14] and [17] can be regarded as special cases of the proposed cost function.

Using matrix notation, the cost function $E(O)$ can be rewritten as

$$\lambda(O - X)^T(O - X) + (D_x O - V^h)^T(D_x O - V^h)$$
$$+ (D_y O - V^v)^T(D_y O - V^v), \qquad (11)$$

where the matrices D_x and D_y are discrete differentiation operators.

The vector O that minimizes the cost function is uniquely defined as the solution of the linear equation

$$(\lambda I + D_x^T D_x + D_y^T D_y)O = \lambda X + D_x^T V^h + D_y^T V^v, \qquad (12)$$

where I is an identity matrix. It can be easily verified that the matrix $(\lambda I + D_x^T D_x + D_y^T D_y)$ is non-singular if λ is positive while the matrix $(D_x^T D_x + D_y^T D_y)$ is singular. Thus, a fast separating method like the method in [18] is applicable to solve the above linear equation due to the non-singularity of the matrix $(\lambda I + D_x^T D_x + D_y^T D_y)$ with a positive λ. However, the separating method in [18] is not applicable if the value of λ is 0. This is because that the matrix $(D_x^T D_x + D_y^T D_y)$ is singular. Thus, it is much easier to solve the proposed optimization problem based on the cost function (10) than the optimization problem in [14].

As an illustration, the structure transfer filter is applied to estimate the transmission map of a haze image. As shown in Fig. 6, the structure of the haze image is indeed transferred to the simplified dark channel by the structure transfer filter. Even though the structure of the vector field V is transferred into the output image O^* by the structure transfer filter, the output image O^* sometimes needs to be smoothed. An example is given in Fig. 7. Clearly, the quality of
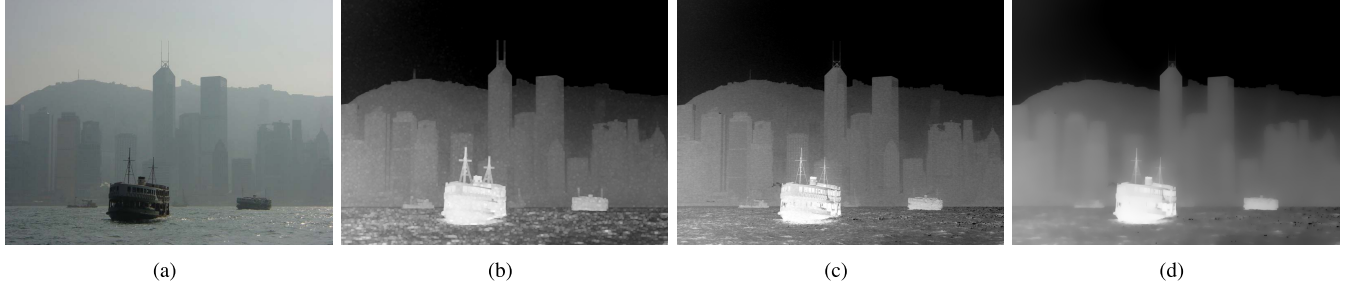
Fig. 6. Illustration of the proposed G-GIF by using it to estimate the transmission map of a haze image. (a) a haze image; (b) simplified dark channel of the normalized haze image which is the image to be filtered; (c) output image of the structure transfer filter; and (d) output image of the proposed G-GIF.
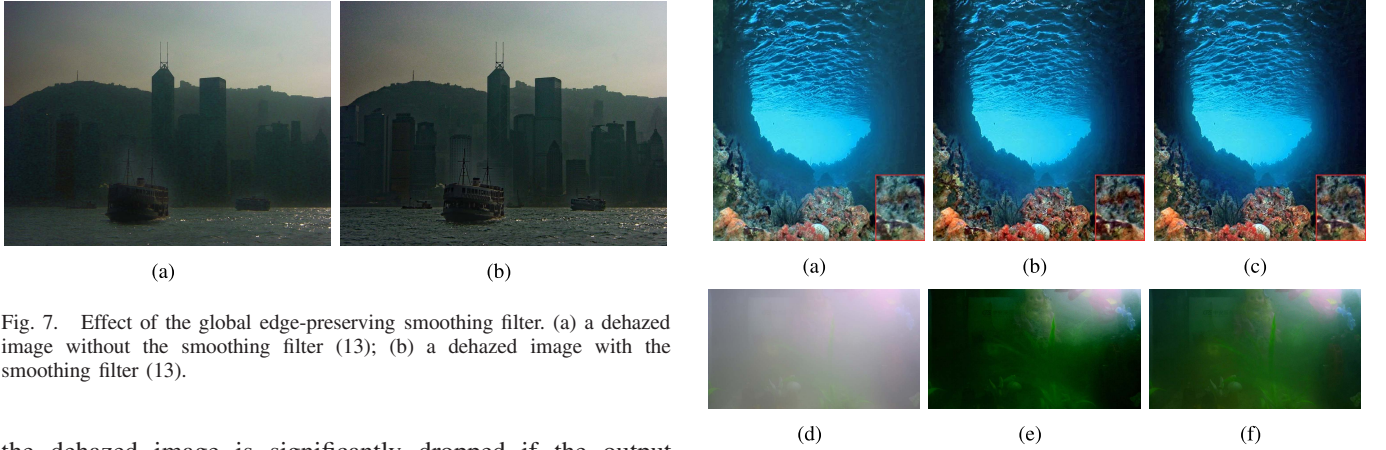

Fig. 7. Effect of the global edge-preserving smoothing filter. (a) a dehazed image without the smoothing filter (13); (b) a dehazed image with the smoothing filter (13).

Fig. 8. Two images and their enhanced images via two different decomposition models. (a) an underwater image; (b) an enhanced image via the decomposition model in [11]; and (c) an enhanced image via the proposed model. (d) a haze image; (e) an enhanced image via the decomposition model in [11]; and (f) an enhanced image via the proposed model. The color is slightly over-saturated by the model in [11].

the dehazed image is significantly dropped if the output image O^* is not smoothed. To achieve the objective, the output image O^* is decomposed into two layers via an edge-preserving smoothing filter. Inspired by the WLS filter in [16] and the quadratic optimization problem in [17], a new edge-preserving smoothing filter is formulated as

$$\min_{\varphi} \sum_p [(\varphi(p) - O^*(p))^2 + \gamma \left(\frac{(\frac{\partial \varphi(p)}{\partial x})^2}{|V^h(p)|^\theta + \epsilon} + \frac{(\frac{\partial \varphi(p)}{\partial y})^2}{|V^v(p)|^\theta + \epsilon} \right)], \tag{13}$$

where γ, θ, and ϵ are three constants.

As shown in the Equation (13), the inputs of the edge-preserving smoothing filter are an image to be smoothed and a vector field. It can be easily checked that when the vector field is given by

$$V^h(p) = \frac{\partial O^*(p)}{\partial x}; \quad V^v(p) = \frac{\partial O^*(p)}{\partial y}, \tag{14}$$

the proposed cost function in Equation (13) is the same as the cost function in [16]. This implies that the WLS filter in [16] is a special case of the proposed one.

Similarly, using the matrix notation, the above cost function can be rewritten as

$$(\varphi - O^*)^T (\varphi - O^*) + \gamma (\varphi^T D_x^T B_x D_x \varphi + \varphi^T D_y^T B_y D_y \varphi),$$

where the matrices B_x and B_y are given as

$$B_x = \text{diag}\{ \frac{1}{|V^h(p)|^\theta + \epsilon} \}; \quad B_y = \text{diag}\{ \frac{1}{|V^v(p)|^\theta + \epsilon} \}. \tag{15}$$

The vector φ that minimizes the cost function is uniquely defined as the solution of the linear equation

$$(I + \gamma (D_x^T B_x D_x + D_y^T B_y D_y)) \varphi = O^*. \tag{16}$$

Similarly, by using a fast separate method like the method in [18], the above linear equation can be solved very fast. As shown in [18], the speed of the fast WLS is almost the same as those of the GIF in [7] and the WGIF in [9]. The speeds of both the proposed structure filter and the edge-preserving smoothing filter are comparable to the speed of the fast WLS. Therefore, the complexity of the proposed G-GIF is about the double of the GIF in [7] and the WGIF in [9]. In the next section, the proposed G-GIF will be applied to design a single image haze removal algorithm.

IV. SINGLE IMAGE HAZE REMOVAL VIA THE G-GIF

In this section, a simple single image haze removal algorithm is introduced by using the proposed G-GIF and the Koschmiedars law [22]. The global atmospheric light $A_c(c \in \{r, g, b\})$ is empirically determined by using a hierarchical searching method based on the quad-tree subdivision [23]. The value of the transmission map $t(p)$ is then
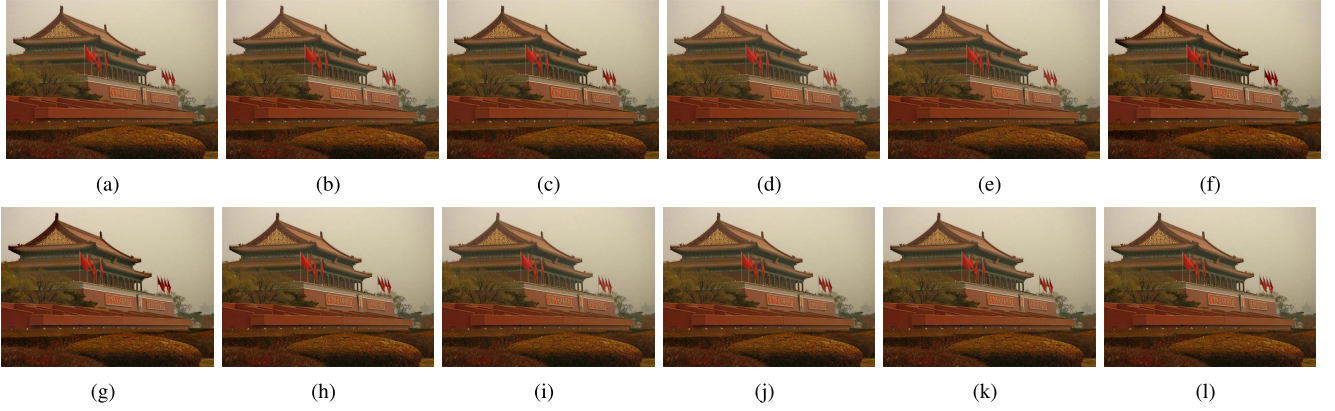
Fig. 9. Different choices of λ in the equation (24) as well as γ, θ, and ϵ in the equation (25). (a) $\lambda = 1/2048$; (b) $\lambda = 1/512$; (c) $\lambda = 1/8192$; (d) $\gamma = 512$; (e) $\gamma = 1024$; (f) $\gamma = 8192$; (g) $\theta = 1$; (h) $\theta = 1.5$; (i) $\theta = 2$; (j) $\epsilon = 1/32$; (k) $\epsilon = 1/128$; and (l) $\epsilon = 1/256$.

estimated by using the proposed G-GIF. Finally, the scene radiance $Z(p)$ is recovered.

According to the Koschmiedars law [22], a haze image is generally modeled by

$$X_c(p) = Z_c(p)t(p) + A_c(1 - t(p)), \quad (17)$$

where $c \in \{r, g, b\}$ is a color channel index, X_c is a haze image, Z_c is a haze-free image, A_c is the global atmospheric light, and t is the medium transmission describing the portion of the light that is not scattered and reaches the camera.

Unlike the decomposition model in [11], it is assumed that the values of A_r, A_g and A_b are estimated before the simplified dark channel is computed. Fortunately, this is not problem by using the method in [23] to estimate the values of A_r, A_g and A_b. It should be pointed out that the methods in [6], [7], and [9] are not applicable because the global atmospheric light is needed to estimate before the dark channel is computed.

A simple haze image model is derived by using the simplified dark channels of the normalized haze image X/A and the normalized haze-free image Z/A. Let $\tilde{X}_m(p)$ and $\tilde{Z}_m(p)$ be defined as

$$\tilde{X}_m(p) = \min\{\frac{X_r(p)}{A_r}, \frac{X_g(p)}{A_g}, \frac{X_b(p)}{A_b}\}, \quad (18)$$

$$\tilde{Z}_m(p) = \min\{\frac{Z_r(p)}{A_r}, \frac{Z_g(p)}{A_g}, \frac{Z_b(p)}{A_b}\}, \quad (19)$$

$\tilde{X}_m$ and $\tilde{Z}_m$ are called the minimal color components of the images $\frac{X}{A}$ and $\frac{Z}{A}$, respectively [11], [19]–[21]. Since the transmission map $t(p)$ is independent of the color channels r, g, and b, it can be derived from the haze image model in Equation (17) that the relationship between the minimal color components $\tilde{X}_m$ and $\tilde{Z}_m$ is given as

$$\tilde{X}_m(p) = (1 - t(p)) + \tilde{Z}_m(p)t(p). \quad (20)$$

Let $\Omega_\zeta(p)$ be a square window centered at the pixel p of a radius ζ. The simplified dark channels of the normalized images $\frac{X}{A}$ and $\frac{Z}{A}$ are then defined as [9]

$$J_d^{\tilde{Z}}(p) = \min_{p' \in \Omega_\zeta(p)}\{\tilde{Z}_m(p')\}, \quad (21)$$

$$J_d^{\tilde{X}}(p) = \min_{p' \in \Omega_\zeta(p)}\{\tilde{X}_m(p')\}, \quad (22)$$

where the value of ζ is fixed at 7 in this paper.

Since the value of $t(p)$ is usually constant in the neighborhood $\Omega_\zeta(p)$, it can be derived from Equation (20) that

$$J_d^{\tilde{X}}(p) = (1 - t(p)) + J_d^{\tilde{Z}}(p)t(p). \quad (23)$$

Compared with the decomposition model in [11], the model in the Equation (23) can be applied to improve the robustness of single image haze removal algorithm as shown in Fig. 8. For example, the color is slightly over-saturated by the model in [11] as shown in Fig. 8(e) and the zoom-in region in Fig. 8(b). The problem is overcome by the proposed decomposition model as illustrated in Fig. 8(f) and the zoom-in region in Fig. 8(c).

The image to be filtered is $J_d^{\tilde{X}}$ and the guidance vector field is defined as $\nabla \tilde{X}_m$. The structure of $\nabla \tilde{X}_m$ is transferred to the image $J_d^{\tilde{X}}$ via

$$\min_O \{\lambda E_1(O, J_d^{\tilde{X}}) + E_2(O, \nabla \tilde{X}_m)\}, \quad (24)$$

where the value of λ is selected as 1/2048 for all the experimental results in this paper provided that its value is specified.

The output image O^* is further smoothed as

$$\min_\varphi \sum_p [(\varphi(p) - O^*(p))^2 + \gamma(\frac{(\frac{\partial \varphi(p)}{\partial x})^2}{|\frac{\partial \tilde{X}_m(p)}{\partial x}|^\theta + \epsilon} + \frac{(\frac{\partial \varphi(p)}{\partial y})^2}{|\frac{\partial \tilde{X}_m(p)}{\partial y}|^\theta + \epsilon})], \quad (25)$$

where the values of γ, θ, and ϵ are respectively selected as 2048, 13/8, and 1/64 for all the experimental results in this paper provided that their values are specified.

The optimal value of the transmission map $t(p)$ is then computed as

$$t^*(p) = 1 - \varphi^*(p). \quad (26)$$

Similar to the algorithm in [11], the proposed algorithm includes an adaptive sky-region compensation term to detect sky region in a haze image. The value of transmission map is further tuned in the sky region to avoid amplifying noise in the sky region.

Finally, the scene radiance $Z(p)$ is recovered by

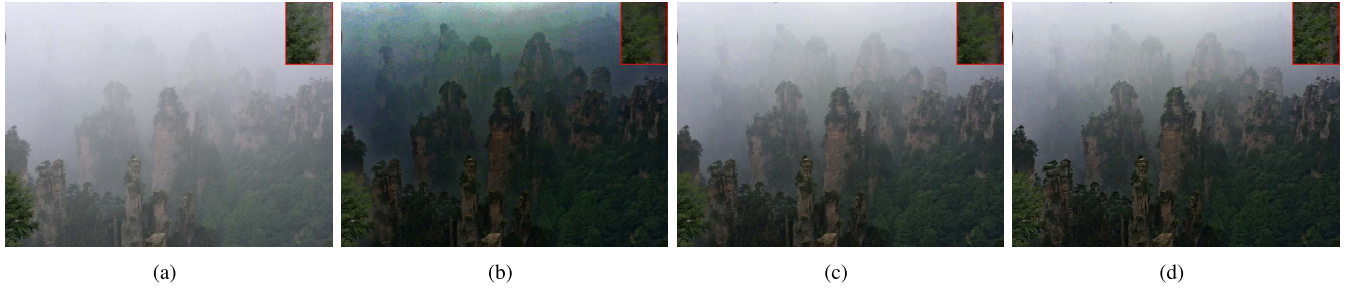$$Z_c(p) = \frac{X_c(p) - A_c}{t^*(p)} + A_c. \quad (27)$$

Fig. 10.   Comparison of the proposed G-GIF with the GIF in [7] and the WGIF in [9]. (a) a hazed image; (b) a de-hazed image by the GIF in [7]; (c) a de-hazed images by the WGIF in [9]; (d) a de-hazed image by the proposed G-GIF. The proposed G-GIF preserves the structure of branches and leafs better than the GIF and WGIF.
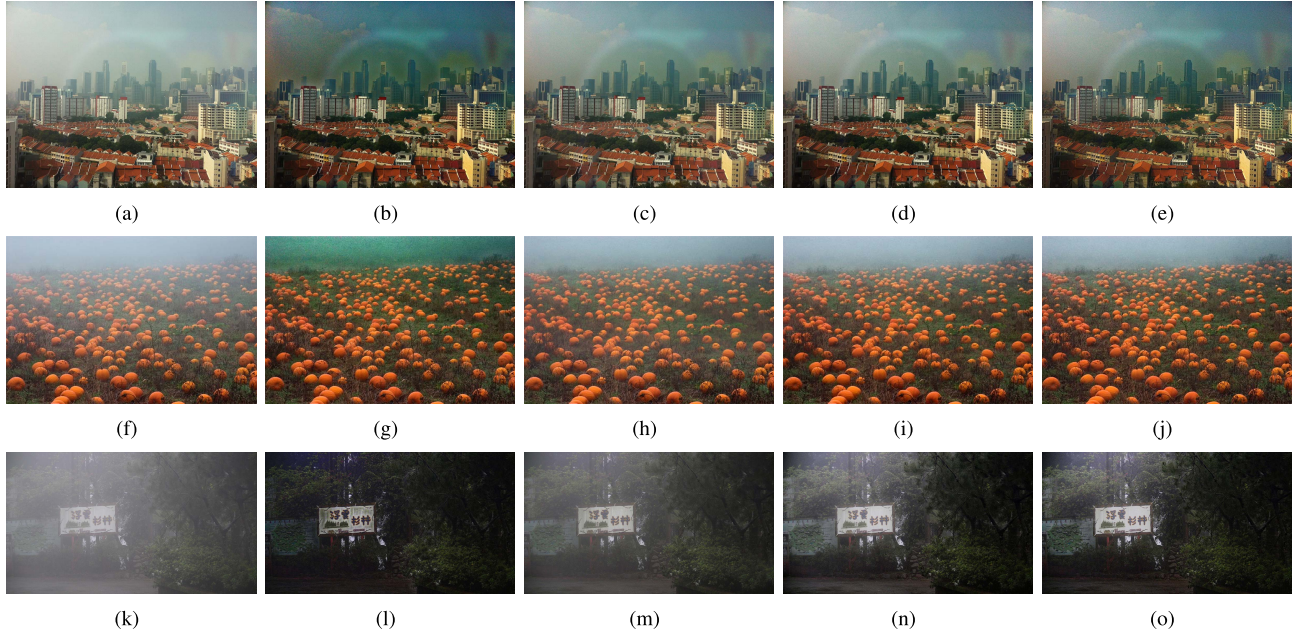

Fig. 11.   Comparison of the proposed haze removal algorithm and the haze removal algorithms in [7], [8], and [11] via three haze images. (a, f, k) three images with haze; (b, g, l) de-hazed images by the algorithm in [7]; (c, h, m) de-hazed images by the algorithm in [8]; (d, i, n) de-hazed images by the algorithm in [11]; (e, j, o) de-hazed images by the proposed algorithm.

V. EXPERIMENTAL RESULTS

In this section, different choices of λ in the Equation (24) as well as γ, θ, and ϵ in the Equation (25) are first tested. It is shown in Fig. 9 that the proposed G-GIF is not sensitive to the choices of λ in the Equation (24) as well as γ, θ, and ϵ in the Equation (25).

The proposed G-GIF is also compared with the GIF in [7] and the WGIF in [9] by using them to study single image haze removal. It is shown in Fig. 10 that the proposed G-GIF preserves the structure of branches and leafs better than the GIF and WGIF. It is also illustrated in Fig. 1 that the proposed G-GIF preserves the structure of hair of the human subject better than the GIF and WGIF. Therefore, the proposed G-GIF preserves fine structure better than the GIF and WGIF.

The proposed haze removal algorithm is then compared with three state-of-the-art haze removal algorithms in [7], [8], and [11] by testing three haze images. The guidance image is selected as the minimal color channel of the haze image for all the algorithms in [7], [8], and [11]. All the settings
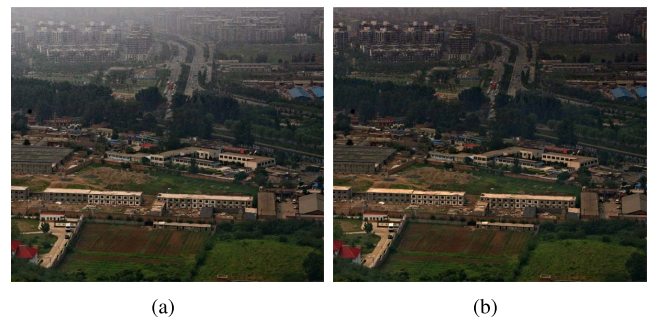

Fig. 12.   Limitation of the proposed haze removal algorithm. (a) a dehazed image by the proposed algorithm; and (b) a dehazed image by reducing the haze level via an interactive mode.

of the parameters are selected according to the algorithms in [7], [8], and [11]. It is demonstrated in Fig. 11 that the algorithm in [7] removes haze better than other haze removal algorithms but it amplifies noise in brightest regions. It is demonstrated in Figs. 11 that the algorithm in [8] preforms
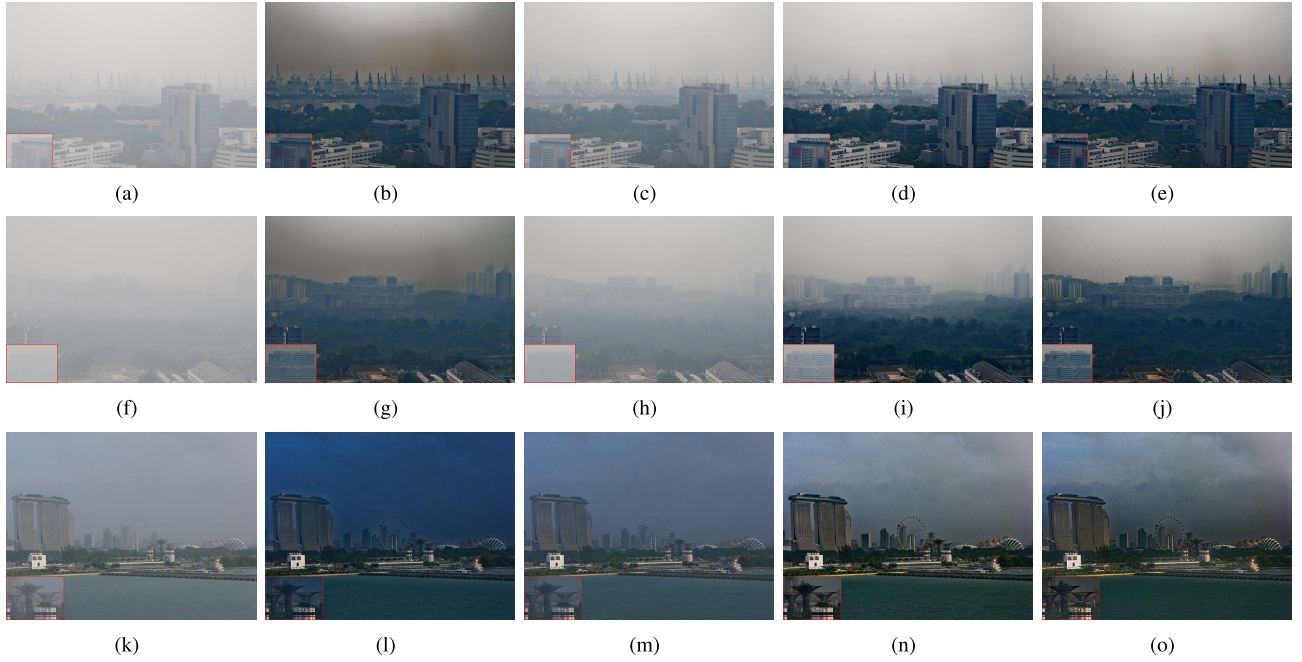
Fig. 13. Comparison of the proposed haze removal algorithm and the haze removal algorithms in [7], [8], [11] via three haze images with large sky regions. (a, f, k) four images with haze; (b, g, l) de-hazed images by the algorithm in [7]; (c, h, m) de-hazed images by the algorithm in [8]; (d, i, n) de-hazed images by the algorithm in [11]; (e, j, o) de-hazed images by the proposed algorithm.

well when the haze is not heavy but the haze is not removed well when the haze is heavy. This is because that the values of α and the coefficients of the linear model are fixed in [8]. Their values should be adaptive to the haze degree of the input image. It is worth noting that it is challenging to estimate the values of α and the coefficients of the linear model for the algorithm in [8]. Both the algorithm in [11] and the proposed algorithm include an adaptive sky-region compensation term to detect sky region in a haze image and the value of transmission map is tuned in the sky region to avoid amplifying noise in the sky region. A drawback of the sky-region compensation term is that the haze might not removed well if there is no sky region in a haze image as shown in Fig. 11. This is a limitation of the proposed haze removal algorithm. The problem could be addressed by introducing an interactive mode to the proposed algorithm which allows a user to enable or disable the sky-region compensation term according to her/his preference as shown in Fig. 12. Since only the operation in the Equation (27) is repeated in the interactive mode, the interactive mode in our dehazing apps on smart phones runs in real time.

All these four haze removal algorithms are also compared by testing three haze images with large sky regions. It is shown in Fig. 13 that the algorithm in [7] usually removes haze better than other algorithms while it also amplified noises in the sky regions. The quality of dehazed images by the proposed algorithm is better than the quality of dehazed images by the algorithm in [11] in the senses that the dehazed images by the proposed algorithm are sharper than those dehazed images by the algorithm in [11] as demonstrated in Figs. 11(d), 11(i), 13(d), 13(i), and 13(n), and the fine structure is preserved better by the proposed algorithm as shown in Figs. 11(e), 11(j), 13(e), 13(j), and 13(o). This is

TABLE I

COMPARISON OF PERCEPTUAL FOG DENSITY

Image	[7]	[8]	[11]	Proposed	Haze
Fig.11(a)	**0.255**	0.424	0.354	0.301	0.658
Fig.11(f)	**0.194**	0.411	0.313	0.278	0.567
Fig.11(k)	**0.417**	1.185	0.518	0.423	2.305
Fig.13(a)	0.992	3.293	1.402	**0.937**	7.447
Fig.13(f)	1.066	4.568	1.181	**0.836**	9.259
Fig.13(k)	**0.399**	0.835	0.535	0.437	2.28
Average	0.554	1.786	0.717	**0.535**	2.815

because that the WGIF over smoothes the dehazed images, especially in the areas of fine structures. The problem is overcome by the proposed G-GIF.

The no-reference perceptual fog density assessment metric D in [1] is also adopted to compare the four haze removal algorithms. The metric in [1] does not require the original foggy image. A lower value of D implies better defogging performance. It is demonstrated in Table I that the algorithm in [7] is ranked the first for four images and the proposed algorithm is ranked the first for two images. The proposed algorithm is ranked the first on average. Both the haze removal algorithm in [11] and the proposed haze removal algorithm include the adaptive sky-region compensation term. Clearly, the experimental results in Table I show that the proposed G-GIF indeed outperforms the WGIF.

Overall, the proposed algorithm preserves details in regions of fine structure visibly better than the algorithms in [7], [8], [11]. On the other hand, since the proposed G-GIF is composed of a structure transfer filter and an edge-preserving

smoothing filter. The speed of the proposed algorithm is about double of the algorithms in [7], [8], and [11]. Therefore, the proposed algorithm is more suitable for applications on PC.

VI. CONCLUSION AND DISCUSSION

A new globally guided image filtering is introduced in this paper. The proposed filter can be applied to produce sharper images and preserves details in regions of fine structure visibly better than the existing locally guided image filtering. It is applied to study single image haze removal. Experimental results demonstrate that the proposed haze removal algorithm indeed improves visual quality of dehazed images.

Besides single image haze removal, there are many applications of the proposed filters. For example, the filter can be applied to study panorama imaging [24], edge-aware smoothing pyramid for exposure fusion [25], detail enhancement, image matting, HDR compression, feathering, high resolution up-sampling, and so on. We will study these applications in our future research.

REFERENCES

[1] L. K. Choi, J. You, and A. C. Bovik, "Referenceless prediction of perceptual fog density and perceptual image defogging," *IEEE Trans. Image Process.*, vol. 24, no. 11, pp. 3888–3901, Nov. 2015.

[2] S. G. Narasimhan and S. K. Nayar, "Chromatic framework for vision in bad weather," in *Proc. IEEE Conf. Comput. Vis. Pattern Recognit. (CVPR)*, Hilton Head Island, SC, USA, Jun. 2000, pp. 598–605.

[3] R. Tan, "Visibility in bad weather from a single image," in *Proc. IEEE Conf. Comput. Vis. Pattern Recognit. (CVPR)*, Anchorage, AK, USA, Jun. 2008, pp. 1–8.

[4] R. Fattal, "Single image dehazing," in *Proc. SIGGRAPH*, New York, NY, USA, Jun. 2008, pp. 1–9.

[5] P. S. Chavez, "An improved dark-object subtraction technique for atmospheric scattering correction of multispectral data," *Remote Sens. Environ.*, vol. 24, no. 3, pp. 459–479, Apr. 1988.

[6] K. He, J. Sun, and X. Tang, "Single image haze removal using dark channel prior," *IEEE Trans. Pattern Anal. Mach. Intell.*, vol. 33, no. 12, pp. 2341–2353, Dec. 2011.

[7] K. He, J. Sun, and X. Tang, "Guided image filtering," *IEEE Trans. Pattern Anal. Mach. Intell.*, vol. 35, no. 6, pp. 1397–1409, Jun. 2013.

[8] Q. Zhu, J. Mai, and L. Shao, "A fast single image haze removal algorithm using color attenuation prior," *IEEE Trans. Image Process.*, vol. 24, no. 11, pp. 3522–3533, Nov. 2015.

[9] Z. Li, J. Zheng, Z. Zhu, W. Yao, and S. Wu, "Weighted guided image filtering," *IEEE Trans. Image Process.*, vol. 24, no. 1, pp. 120–129, Jan. 2015.

[10] F. Kou, W. Chen, C. Wen, and Z. Li, "Gradient domain guided image filtering," *IEEE Trans. Image Process.*, vol. 24, no. 11, pp. 4528–4539, Nov. 2015.

[11] Z. Li and J. Zheng, "Edge-preserving decomposition-based single image haze removal," *IEEE Trans. Image Process.*, vol. 24, no. 12, pp. 5432–5441, Dec. 2015.

[12] J. Park, H. Kim, Y. W. Tai, M. S. Brown, and I. Kweon, "High quality depth map upsampling for 3D-TOF cameras," in *Proc. IEEE Int. Conf. Comput. Vis.*, Colorado Springs, CO, USA, Jun. 2011, pp. 1623–1630.

[13] R. Fattal, D. Lischinski, and M. Werman, "Gradient domain high dynamic range compression," *ACM Trans. Graph.*, vol. 27, no. 3, pp. 67-1–67-10, Jul. 2002.

[14] P. Pérez, M. Gangnet, and A. Blake, "Poisson image editing," *ACM Trans. Graph.*, vol. 22, no. 3, pp. 313–318, Jul. 2003.

[15] E. S. L. Gastal and M. M. Oliveira, "Domain transform for edge-aware image and video processing," *ACM Trans. Graph.*, vol. 30, no. 4, Jul. 2011, Art. no. 69.

[16] Z. Farbman, R. Fattal, D. Lischinski, and R. Szeliski, "Edge-preserving decompositions for multi-scale tone and detail manipulation," *ACM Trans. Graph.*, vol. 27, no. 3, p. 67, Aug. 2008.

[17] Z. G. Li, J. H. Zheng, and S. Rahardja, "Detail-enhanced exposure fusion," *IEEE Trans. Image Process.*, vol. 21, no. 11, pp. 4672–4676, Nov. 2012.

[18] D. Min, S. Choi, J. Lu, B. Ham, K. Sohn, and M. Do, "Fast global image smoothing based on weighted least squares," *IEEE Trans. Image Process.*, vol. 23, no. 12, pp. 5638–5653, Dec. 2014.

[19] J.-P. Tarel and N. Hautiere, "Fast visibility restoration from a single color or gray level image," in *Proc. IEEE Conf. Comput. Vis. Pattern Recognit.*, Kyoto, Japan, Sep./Oct. 2009, pp. 2201–2208.

[20] S. Kang, W. Bo, Z. Zhihui, and Z. Zhiqiang, "Fast single image dehazing using iterative bilateral filter," in *Proc. Int. Conf. Inf. Eng. Comput. Sci.*, Wuhan, China, Dec. 2010, pp. 1–4.

[21] C. Xiao and J. Gan, "Fast image dehazing using guided joint bilateral filter," *Vis. Comput.*, vol. 28, nos. 6–8, pp. 713–721, Jun. 2012.

[22] H. Koschmider, "Theorie der horizontalen sichtweite," *Contrib. Phys. Free Atmos.*, vol. 12, pp. 171–181, 1924.

[23] J.-H. Kim, W.-D. Jang, J.-Y. Sim, and C.-S. Kim, "Optimized contrast enhancement for real-time image and video dehazing," *J. Vis. Commun. Image Represent.*, vol. 24, no. 3, pp. 410–425, Apr. 2013.

[24] W. Yao and Z. Li, "Instant color matching for mobile panorama imaging," *IEEE Signal Process. Lett.*, vol. 22, no. 1, pp. 6–10, Jan. 2015.

[25] Z. Li, Z. Wei, C. Wen, and J. Zheng, "Detail-enhanced multi-scale exposure fusion," *IEEE Trans. Image Process.*, vol. 26, no. 3, pp. 1243–1252, Mar. 2017.

Zhengguo Li (SM'03) received the B.Sc. and M.Eng. degrees from Northeastern University, Shenyang, China, in 1992 and 1995, respectively, and the Ph.D. degree from the Nanyang Technological University, Singapore, in 2001. Since 2002, he has been actively involved in the development of H.264/AVC and HEVC. He had three informative proposals adopted by the H.264/AVC and three normative proposals adopted by the HEVC. He is currently with the Agency for Science, Technology and Research, A*STAR, Singapore. He has co-authored one monograph, over 200 journal/conference papers including 40 IEEE Transactions, and ten granted USA patents, including normative technologies on scalable extension of H.264/AVC and HEVC. His current research interests include computational photography, mobile imaging, video processing and delivery, and switched and impulsive control. He is a member of SIG on computational imaging. He served the General Chair of the IEEE ICIEA in 2016, the Technical Brief Co-Founder of SIGGRAPH Asia, the General Co-Chair of CCDC in 2013, the Leading Workshop Chair of the IEEE ICME in 2013, and an Area Chair of the IEEE ICIP 2016. From 2014 to 2016, he was an Associate Editor of the IEEE SIGNAL PROCESSING LETTERS. Since 2016, he has been an Associate Editor of the IEEE TRANSACTIONS ON IMAGE PROCESSING.

Jinghong Zheng (S'02–M'09) received the B.Sc. degree in electronic engineering from the Beijing Institute of Technology, Beijing, China, in 2000, and the Ph.D. degree in electronic and electrical engineering from Nanyang Technological University, Singapore, in 2006. Since 2006, she has been a Scientist with the Institute for Infocomm Research, A*STAR, Singapore. She is currently with the Energy Department, Smart Energy and Environment Cluster. Her research interests include forecasting of solar energy, high dynamic range image processing, image fusion and enhancement, in painting, error concealment/resilience of H.264 video, region of interesting video coding, scalable video coding, and video streaming.